The Tailored Surface Oxygen Vacancies and Reduced Optical Band Gap of NiO During the Development of NiO@Polyaniline Hybrid Materials for the Efficient Asymmetric and Oxygen Evolution Reaction Applications

Fida Hussain, Wanhinyal Dars, Rabia Kanwal, Jethanand Parmar, Ghansham Das, Ahmed Raza, Haresh Kumar, Rameez Mangi, Masroor Ali Bhellar, Ambedker Meghwar, et al.

catalysts

MDPI

Article

The Tailored Surface Oxygen Vacancies and Reduced Optical Band Gap of NiO During the Development of NiO@Polyaniline Hybrid Materials for the Efficient Asymmetric and Oxygen Evolution Reaction Applications

Fida Hussain [1], Wanhinyal Dars [1], Rabia Kanwal [1], Jethanand Parmar [1], Ghansham Das [1], Ahmed Raza [1], Haresh Kumar [1], Rameez Mangi [1], Masroor Ali Bhellar [1], Ambedker Meghwar [1], Kashif Ali [1], Aneela Tahira [2], Muhammad Ali Bhatti [3], Elmuez Dawi [4,*], Rafat M. Ibrahim [5], Brigitte Vigolo [6] and Zafar Hussain Ibupoto [1,*]

1 Institute of Chemistry, University of Sindh, Jamshoro 76080, Sindh, Pakistan; wanhinyald@gmail.com (W.D.)
2 Institute of Chemistry, Shah Abdul Latif University, Khairpur Mirs 66020, Sindh, Pakistan
3 Centre for Environmental Sciences, University of Sindh, Jamshoro 76080, Sindh, Pakistan
4 Mathematics and Science Department, College of Humanities and Sciences, Ajman University, Ajman P.O. Box 346, United Arab Emirates
5 Physics Department, Faculty of Science, Taibah University, Al-Madaina Al Munawarah 42353, Saudi Arabia
6 CNRS, IJL, University de Lorraine, F-54000 Nancy, France
* Correspondence: e.dawi@ajman.ac.ae (E.D.); zaffar.ibhupoto@usindh.edu.pk (Z.H.I.)

Abstract: This study employed a simple and cost-effective method for developing NiO with reduced optical band gaps that can be combined with nanostructured polyaniline (PANI). The composite systems were used as electrocatalytic and electrode materials in oxygen evolution reactions (OER) and in supercapacitor applications. We prepared the composite material in two stages: NiO was prepared with a reduced optical band gap by combining it with wheat peel extract. This was followed by the incorporation of PANI nanoparticles during the chemical oxidation polymerization process. A variety of structural characterization techniques were employed, including scanning electron microscopy (SEM), powder X-ray diffraction (XRD), Fourier transform infrared (FTIR) spectroscopy, UV-visible spectroscopy, and X-ray photoelectron spectroscopy (XPS). A surface-modified NiO/PANI composite with enhanced surface area, fast charge transfer rate, and redox properties was produced. When NiO/PANI composites were tested in KOH electrolytic solution, 0.5 mL of wheat peel extract-mediated NiO/PANI demonstrated excellent electrochemical performance. It was found that the asymmetric supercapacitor (ASC) device had the highest specific capacitance of 404 Fg^{-1} at a current density of 4 Ag^{-1}. In terms of energy density and power density, the ASC device was found to have 140 $Whkg^{-1}$ and 3160 Wkg^{-1}, respectively. The ASC device demonstrated excellent cycling stability and charge storage rates, with 97.9% capacitance retention and 86.9% columbic efficiency. For the OER process, an overpotential of 320 mV was observed at a current density of 10 mA/cm^2. It was found that the NiO/PANI composite was highly durable for a period of 30 h. A proposed hypothesis suggested that reducing the optical band gap of NiO and making its composites with PANI could be an appealing approach to developing next-generation electrode materials for supercapacitors, batteries, and fuel cells.

Keywords: NiO/PANI composite; oxygen evolution reaction; asymmetric supercapacitor device; alkaline solution

Academic Editors: Diana M. Fernandes, Andreia F. Peixoto and Vincenzo Baglio

Received: 27 March 2025
Revised: 14 May 2025
Accepted: 19 May 2025
Published: 22 May 2025

Citation: Hussain, F.; Dars, W.; Kanwal, R.; Parmar, J.; Das, G.; Raza, A.; Kumar, H.; Mangi, R.; Bhellar, M.A.; Meghwar, A.; et al. The Tailored Surface Oxygen Vacancies and Reduced Optical Band Gap of NiO During the Development of NiO@Polyaniline Hybrid Materials for the Efficient Asymmetric and Oxygen Evolution Reaction Applications. *Catalysts* **2025**, *15*, 508. https://doi.org/10.3390/catal15060508

1. Introduction

There is a growing awareness of the importance and necessity of generating and consuming green energy on a global scale. A rapidly growing population, the depletion of fossil fuels, and severe environmental concerns have forced scientists and researchers to reevaluate the commonly used energy sources [1,2]. Consequently, alternative renewable and sustainable energy sources appear to offer a promising solution to these life-threatening challenges posed by conventional energy sources [3]. Due to a greater focus on renewable energy sources and elevating different sectors towards electrification, it is necessary to develop energy storage devices that are efficient and reliable [4]. Among the energy storage systems, supercapacitors have been found to be unique and attractive candidates for these sectors due to their small equivalent series resistance, high power density, long cycling stability, and rapid charge-discharge cycles as compared to conventional batteries, as well as their low operational risk [3]. Due to the variable oxidation states of their electrode materials, supercapacitors exhibit high specific capacitance and energy density compared with electric double layer capacitors [5]. Aside from these advantages, the energy density of supercapacitors is low [6–8]. There are three classes of energy storage devices: faradic, non-faradic, and hybrid. Faradic capacitors (pseudocapacitors) involve reversible redox reactions, whereas non-faradic capacitors are referred to as electric double layer capacitors because energy storage does not occur through redox reactions between electrodes and electrolyte [9]. In contrast, combining faradic and non-faradic processes results in hybrid supercapacitors [10]. The active electrode material is a prerequisite for the efficient electrochemical supercapacitor. Transition metal oxides are among the electrode materials that demonstrate significant pseudocapacitance capabilities due to their rapid reversible faradic reactions with the electrolyte [11,12]. Additionally, transition metal oxides exhibit high energy density when compared to carbon-based electrode materials [11,12]. Their poor stability and electrical conductivity prevent them from being used for commercial purposes [13,14]. As a result of the development of efficient green energy systems [15], alternative, green, and renewable energy sources are becoming increasingly important in order to meet global energy demands [16,17]. It is urgent that active electrocatalysts be developed for oxygen evolution reactions (OER) and hydrogen evolution reactions (HER) as part of the reshaping of alternative green energy. There are a number of processes that can be used for the generation of hydrogen, including biological, thermochemical, solar driven water splitting, and electrochemical water splitting [18–20]. Due to its facile nature and high purity, electrochemical water splitting is considered one of the most suitable technologies to meet energy demands and mitigate environmental concerns by producing oxygen and hydrogen gases [21,22]. Electrochemical water splitting is accomplished by means of two half-cell processes, namely OER and HER. In terms of kinetics, the HER process is simple and requires only two electron transfers, while the OER process requires four electron transfers. Thus, the latter is known as the kinetically sluggish aspect of water splitting; OER has a significant impact on the efficiency of electrochemical water splitting for hydrogen production. A number of electrocatalysts with significant performance have been fabricated and used to lower the desired energy barrier and speed up the OER process [23,24]. A number of precious-metal-based compounds, such as ruthenium oxide (RuO_2) and iridium oxide (IrO_2), have demonstrated excellent catalytic activity for half-cell OER reactions with a minimum overpotential and enhanced active surface area [25,26]. In terms of industrial applications, noble-metal-based electrocatalysts are limited due to their high cost and scarcity in nature. To accelerate the water splitting process for hydrogen and oxygen production, the research in this area focuses on developing low cost and earth-abundant transition-metal-based substances. This has led to intensive studies being conducted for the fabrication of electrocatalysts based on cobalt, nickel, and iron, etc. [27].

The efficiency and durability of these compounds, however, are still far from being commercially viable [28]. Considering the use of nickel-based materials for supercapacitors and OER applications [29,30], it is important to keep in mind their excellent specific capacitance and catalytic activity. Numerous approaches have been proposed to enhance the stability and catalytic properties of nickel-based materials, including heteroatom doping, carbon coating, tailoring the chemical composition, combining with conducting polymers, and altering the shape structure [28,29,31]. This oxide is characterized by its high thermal specific capacitance (3750 F g^{-1}) and wide band gap of 3.8 eV [30]. The nickel-based materials exhibit high catalytic activity, low cost, and excellent stability and durability. Although nickel-based materials have poor electrical conductivity and limited catalytic sites, they cannot be used for developing real-time supercapacitors and electrolyzers for water splitting. In order to explore efficient supercapacitor devices and process OER, more facile and lower cost methods are required to enhance the electrical conductivity, surface area, catalytic sites, and stability of nickel-based materials [32–34]. Therefore, we propose for the first time a strategy for modifying the shape, size, optical band gap, and charge transport of NiO using structure-modifying phytochemicals derived from wheat peel extract. Wheat is a major component of our food supply. A high concentration of phytochemicals is present in wheat peel, and its potential to modify the surface of nanostructured materials has been little investigated. Phytochemicals found in it include cellulose, hemicellulose, lignin, starch, and protein. A polysaccharide such as cellulose or starch can act as a reducing agent, and proteins can serve as structure-directing agents following the synthesis of nanostructured materials. Furthermore, lignin is capable of stabilizing nanostructures. Scheme 1 illustrates the molecular structure of these phytochemicals. In spite of the abundance of reducing agents, such as starch, and structure-directing compounds in wheat peel extracts, these extracts have not been studied for the development of high-performance electrode materials. Furthermore, the combination of surface and optical band gap modified NiO nanostructures with polyaniline may enhance the charge transport and redox properties of composites as an active electrode material for supercapacitors and other applications.

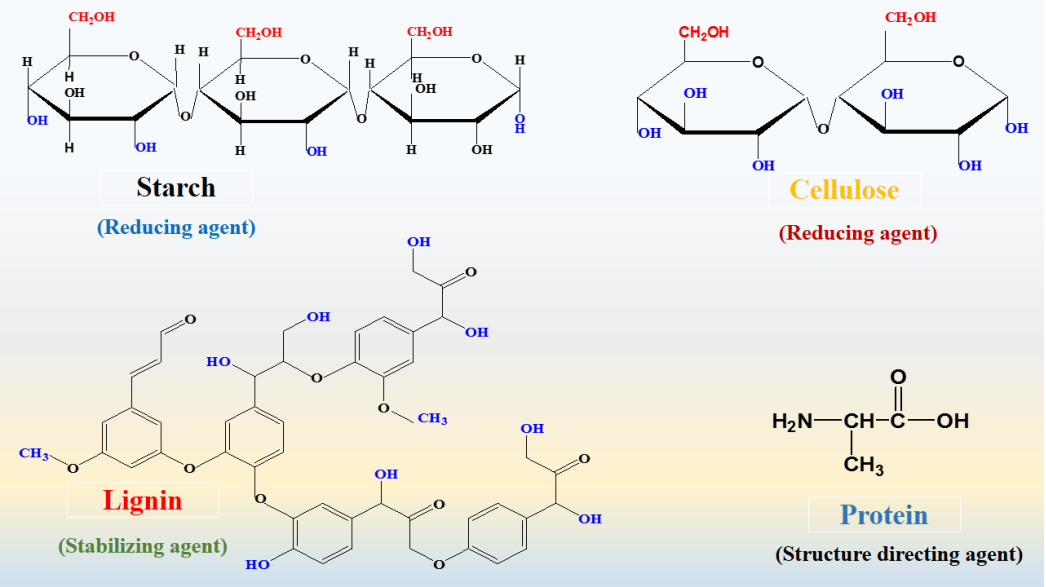

Scheme 1. Chemdraw molecular structure of various phytochemicals from wheat peel extract.

2. Results and Discussion

2.1. Structure, Shape Orientation, Surface Chemical Composition, and Optical Investigations of NiO/PANI Composites

Powder XRD was used to determine the crystal structure of the synthesized NiO/PANI composites (B1, B2), pure NiO (A1), and wheat-peel-extract mediated NiO (A2) by scanning the two-theta angle between 20 and 80°, as shown in Figure 1. The distinctive diffraction patterns for NiO nanoparticles were observed at 37.40° (111), 43.44° (200), and 63.01° (220), indicating a complete demonstration of a cubic phase as verified utilizing JCPD Card No. 01-0.89-7130 [35,36]. It could be seen that the wheat peel extract decreased the relative intensity of diffraction patterns of NiO (A2) due to the reducing nature of starch, which decreased the crystalline properties of NiO. Further, due to the combination of A2 during the synthesis of PANI via chemical oxidation polymerization, the relative intensity was further decreased due to the coverage of PANI over NiO, as shown in Figure 1. It was seen that due to the interaction of polymeric PANI chains with the NiO crystal, NiO patterns were shifted to higher angles. As shown in Figure 2, FTIR was conducted on the synthesized materials to analyze their functional groups. Typical Ni-O stretching vibrations were observed at 653 cm^{-1} and 1146 cm^{-1}, as reported in a previous study [37]. Peaks ranging from 1100 cm^{-1} to 1600 cm^{-1} were correlated with quinonoid and benzenoid vibrational bands. It is noteworthy that the major peaks at 1494 cm^{-1} and 1535 cm^{-1} were associated with C=C and C=N stretching vibrational modes, respectively. Additionally, the peak at 1126 cm^{-1} was assigned to the vibration frequency of the C-N benzenoid ring [38–40]. Comparing the FTIR analysis of bare PANI and pure NiO with NiO/PANI composites revealed certain changes, including a slight shift in frequency, indicating a change in molecular structure. A change in the bonding aspect was also apparent in the intensity of the peaks. An FTIR analysis confirmed significant bonding establishment between PANI macromolecules and NiO nanostructures, indicating the successful formation of NiO/PANI within the polymeric matrix of PANI. Figure 3 illustrates the collection of UV-visible absorbance spectra of various NiO/PANI composites for the purpose of evaluating their optical band gaps. It was observed that NiO/PANI composites exhibit typical absorbance peaks around 372 nm and around 330 nm within the composites, indicating that the composites have been successfully formed. Based on Tauc plots for bare PANI, pure NiO (A1), wheat peel extracts mediated NiO (A2), and composites with PANI as B1 and B2, respectively, as shown in Supplementary Figure S1, the estimated band gaps were calculated to be 2.62 eV, 2.51 eV, 2.47 eV, 2.43 eV, and 2.37 eV, respectively. The band gap depends on the size, shape, and method used for the synthesis of nanostructured material; hence, we observed an optical band gap of pure NiO at 2.62 eV (A1). The optical band gap of NiO (A2) was decreased and estimated as 2.51 eV due to a change in the particle size and shape through the use of wheat peel extract. Further, due to the combination of A2 during the synthesis of PANI via chemical oxidation polymerization process, NiO's optical band gap value decreased to 2.37 eV. Moreover, after combination with PANI, the interface effect between NiO and PANI could be attributed to the reduction of optical band gap. Nanostructured materials have been shown to have an optical band that is affected by their size and shape. There has also been some discussion of these aspects of bandgap reduction in previous studies [41,42]. A decrease in the optical band gap occurs as a result of variations in particle size, shape orientation, and defects during the manufacturing process [42]. The morphology of bare PANI, pure NiO (A1) and A2, and B1 and B2 composite materials was studied via SEM analysis (Figure 4a–e). The bare PANI exhibits an aggregated and continuous aspect (Figure 3a). The shape structure of pure NiO (A1) and its relative composites A2, B1, and B2, consists of thin platelets. The thickness of these sheets is below 100 nm and they have a lateral size of several hundred of microns. When combined with either wheat peel

extract (A2) and/or PANI, a flower-like morphology of interconnected sheets of several microns is observed (Figure 4c–e). The phytochemicals from the wheat peel extract offered abundant oxygenated groups which are probably able to bind with the nickel ions during the growth process and thereby altered the nucleation rate and oriented the NiO into a flower-like shape. Similarly, when NiO or A2 was combined with PANI (B2), the observed flower-like shapes could originate from the successful combination of NiO and PANI within the composite systems. Due to their oxygenated atoms which bind with the nickel ions, phytochemicals such as cellulose and starch play the role of reducing agents and modify the size and surface properties of NiO. Therefore, despite the change in growth kinetics, the size and shape of NiO were dramatically altered. A brief description can be found in Scheme 2 below.

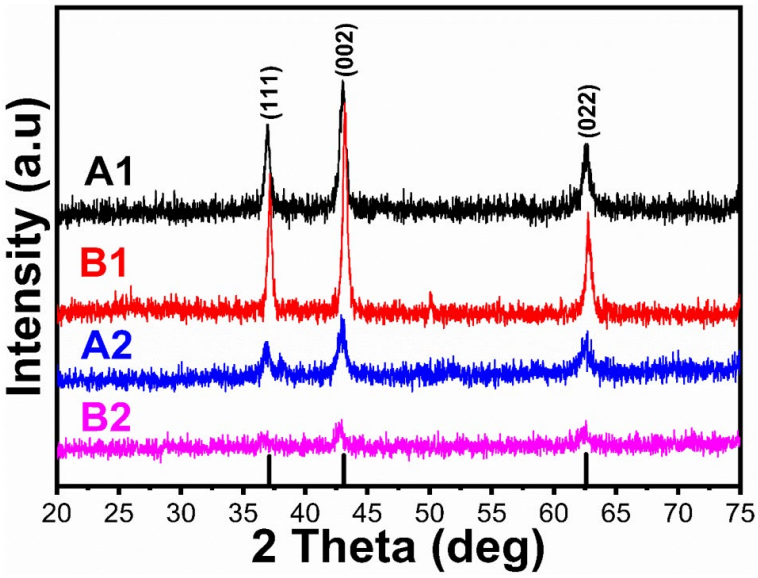

Figure 1. XRD diffraction patterns of bare PANI, pure NiO (A1), wheat-peel-extract mediated NiO (A2), and their corresponding composites with PANI B1 and B2, respectively.

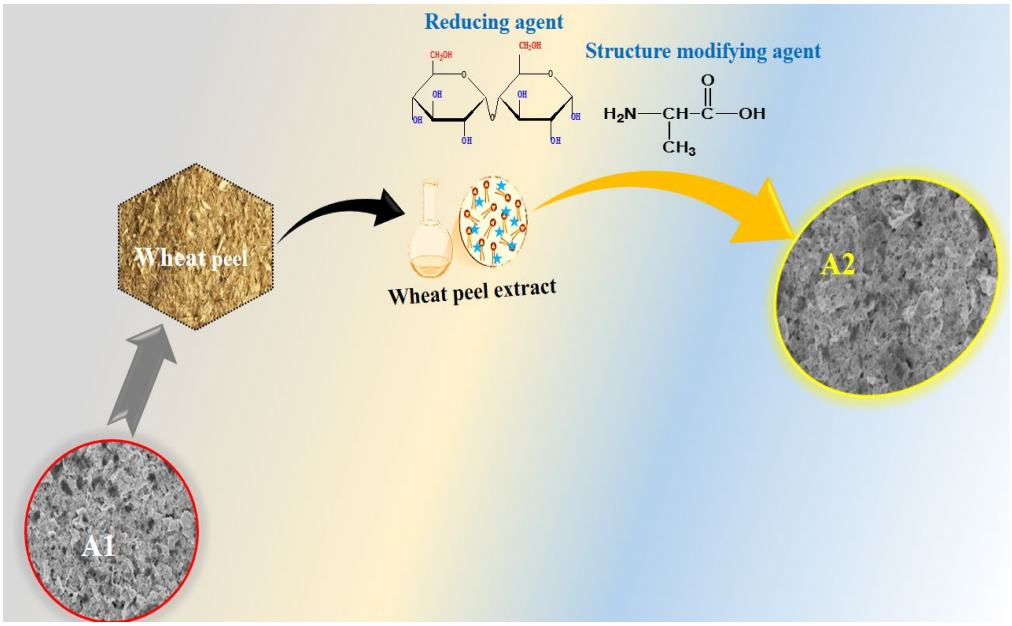

Scheme 2. Synthesis mechanism of NiO nanostructures using wheat peel extract.

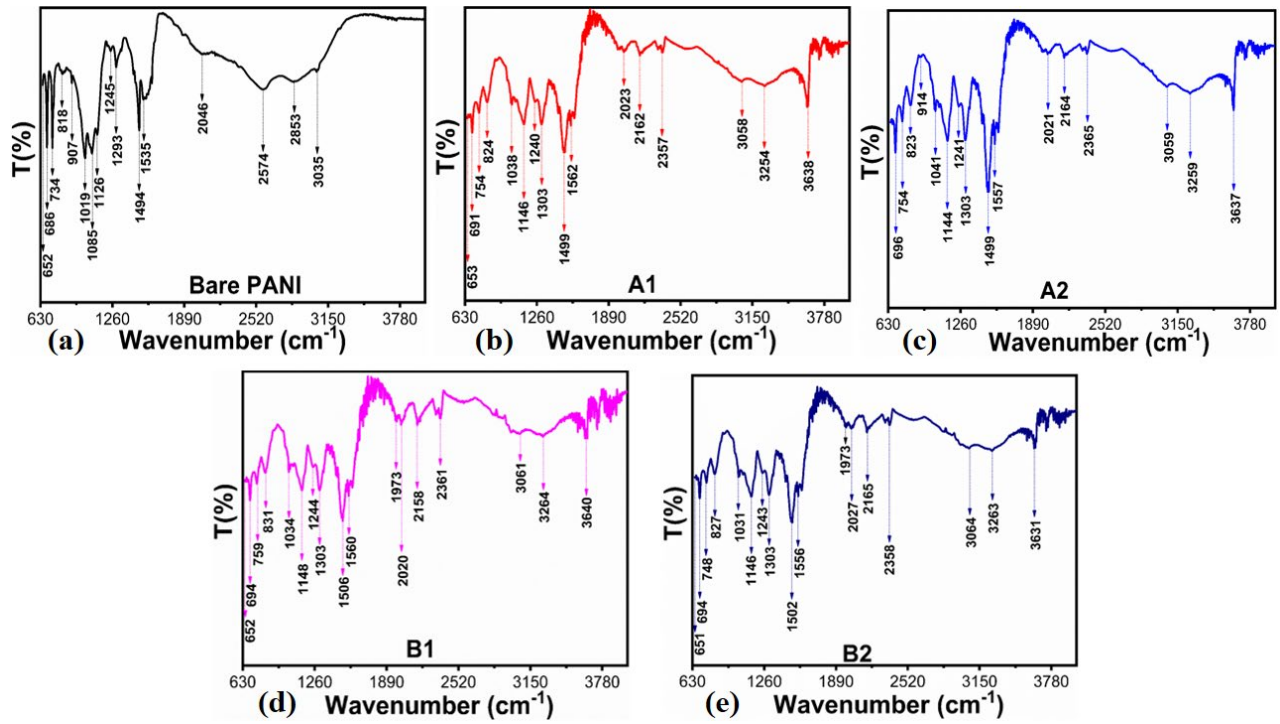

Figure 2. FTIR spectra of (**a**) bare PANI, (**b**) pure NiO (A1), (**c**) wheat-peel-extract mediated NiO (A2), and their corresponding composites with (**d**) PANI B1 and (**e**) B2, respectively.

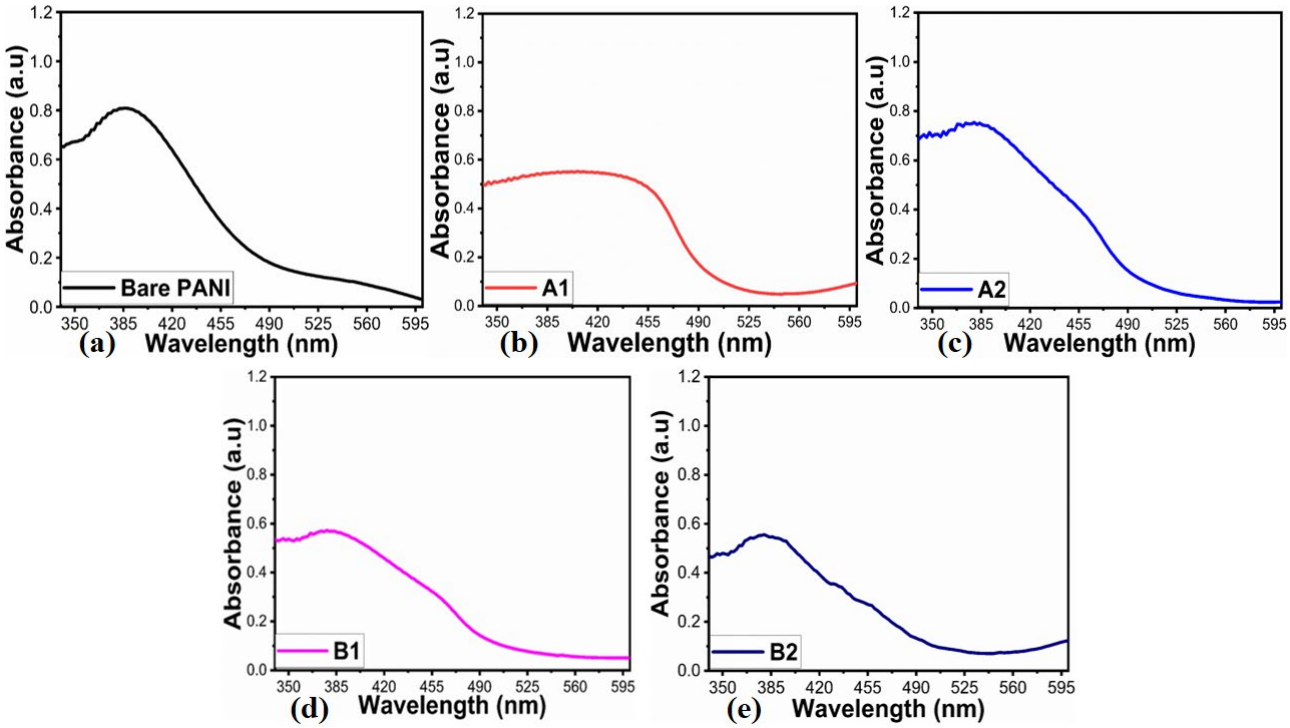

Figure 3. (**a**–**e**) UV-visible absorption spectra of (**a**) bare PANI, (**b**) pure NiO (A1), (**c**) wheat-peel-extract mediated NiO(A2), and (**d**,**e**) their corresponding composites with PANI B1 and B2, respectively.

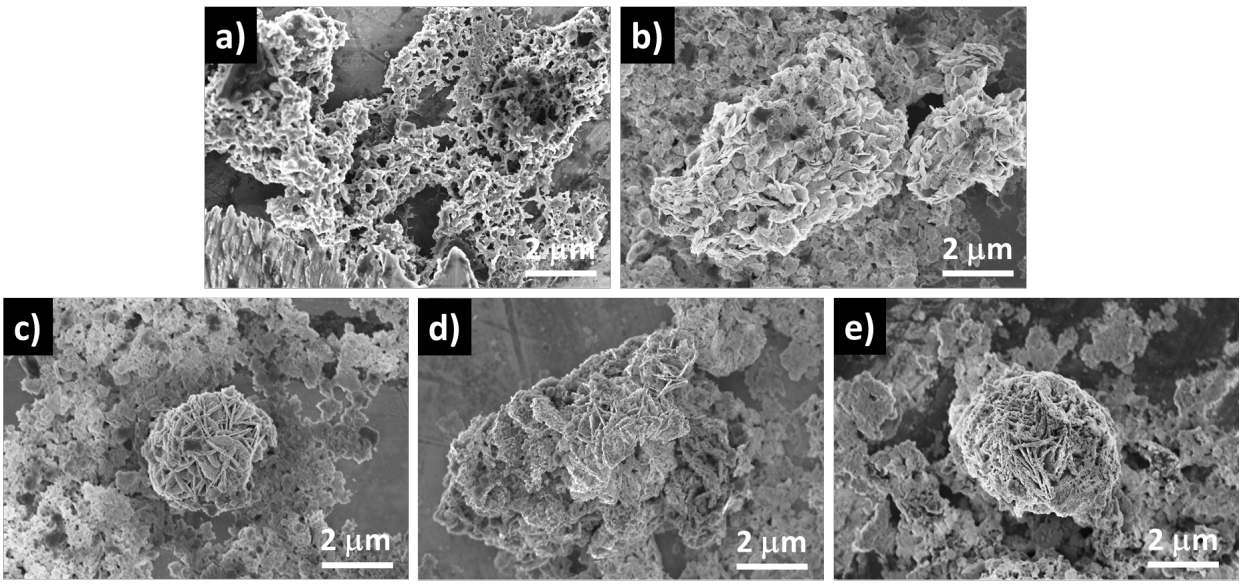

Figure 4. SEM images of (**a**) bare PANI, (**b**) pure NiO (A1), (**c**) NiO/wheat (A2), (**d**) NiO/PANI (B1) and (**e**) A2/PANI (B2) materials.

The expected elements, including C, N, O, and Ni, expected to be present in bare PANI (only C, N, and O), pure NiO (A1), A2, and B2 composite materials are clearly detected in XPS (survey spectra in Supplementary Information Figure S2). Only S, Cl, and Fe impurities come from the used reactants and a possible chemical attack of the laboratory materials. High resolution XPS spectra of Ni2p and O1s features in pure NiO (A1), A2 (NiO prepared with 1 mL of wheat peel extract) and B2 (A2 combined with PANI) composites are shown in Figure 5. For all samples, Ni2p3/2 comprised four main contributions, including two satellite peaks at around 860.8 and 864.7 eV (Figure 5a–c). The two main peaks of Ni2p3/2, located at around 853.7 and 855.4 eV for all the samples, were the typically observed doublet of NiO corresponding to Ni^{2+} and Ni^{3+} environment, respectively [43]. Ni^{2+} is the most common species of NiO, and Ni^{3+} ions are formed from two adjacent Ni^{2+} ions to achieve charge neutrality [44]. The O1s signal was in full agreement with the presence of both Ni^{2+} and Ni^{3+} ions in the three NiO-based samples studied. The O1s signal could be well deconvoluted with three contributions of similar respective concentrations. The components at low energy, centered at around 529.3 eV for all the samples, corresponded to Ni^{2+} ions. The mid-binding energy peak at around 531.2 eV arose from the oxygen vacancies caused by surface OH bonds with Ni^{3+} ions. The peak at higher energy, at around 532.7 eV, is usually associated with the adsorbed oxygen, including absorbed H_2O [43,44]. The B2 sample was observed to have more defects and surface oxygen vacancies that could play a vital role in enhancing electrocatalytic properties. The XPS analysis suggested the presence of NiO and functional groups, which is in complete agreement with FTIR and XRD results.

2.2. Electrochemical Energy Storage Performance Evaluation of Reduced NiO Optical Band Gap and Polyaniline Composites

We investigated the energy storage capacity of synthesized electrode materials using a three-electrode cell setup. In this study, various types of electrode materials were prepared, including bare PANI and nickel foam, pure NiO (A1), 0.5 mL (A2) of wheat-peel-extract mediated NiO, and their composites with polyaniline, denoted as B1 and B2, respectively. A 3 M KOH electrolytic solution was used to evaluate the electrochemical performance of these materials using cyclic voltammetry (CV) and galvanic charge–discharge (GCD). Initially, CV curves were measured at different scan rates for the synthesized electrode

materials. The CV curves of materials such as bare nickel foam, PANI, A1, A2, and B1, B2 at various scan rates can be seen in Figure 6a–f. The oxidation peak of all synthesized samples shifted accordingly: A1 (0.34–0.36), A2 (0.35–0.37), B1 (0.36–0.39) and B2 (0.39–0.42). Because of the faradic processes occurring at the electrode/electrolyte interface, each electrode displayed prominent redox peaks. PANI exhibited intrinsic faradic characteristics, with redox peaks corresponding to the transition from the semiconductor state, Leucoemeraldine, to the conductor state, Emeraldine [45]. Compared to other electrode materials, the peak sizes for the B2 electrode material were enhanced. In response to increasing scan rates, the redox peak current increased linearly, indicating excellent pseudocapacitance behavior and rapid charge transfer rates [46,47]. With increasing scan rates, the oxidation peak and reduction peak shifted toward more positive potentials, respectively, due to the resistance experienced by the electrode materials, as shown in Figure 6a–f. CV analysis demonstrated that the B2 composite electrode exhibited an improved capacitance due to its increased curve area and conductivity compared to other electrodes [47]. According to Figure 6f, the area of the CV curves correlates with specific capacitance [48], indicating that the B2 composite is capable of storing significant amounts of energy. Additionally, the CV analysis revealed that the gradual increase in current response indicates the excellent reversibility and rate capability of the B2 composite electrode.

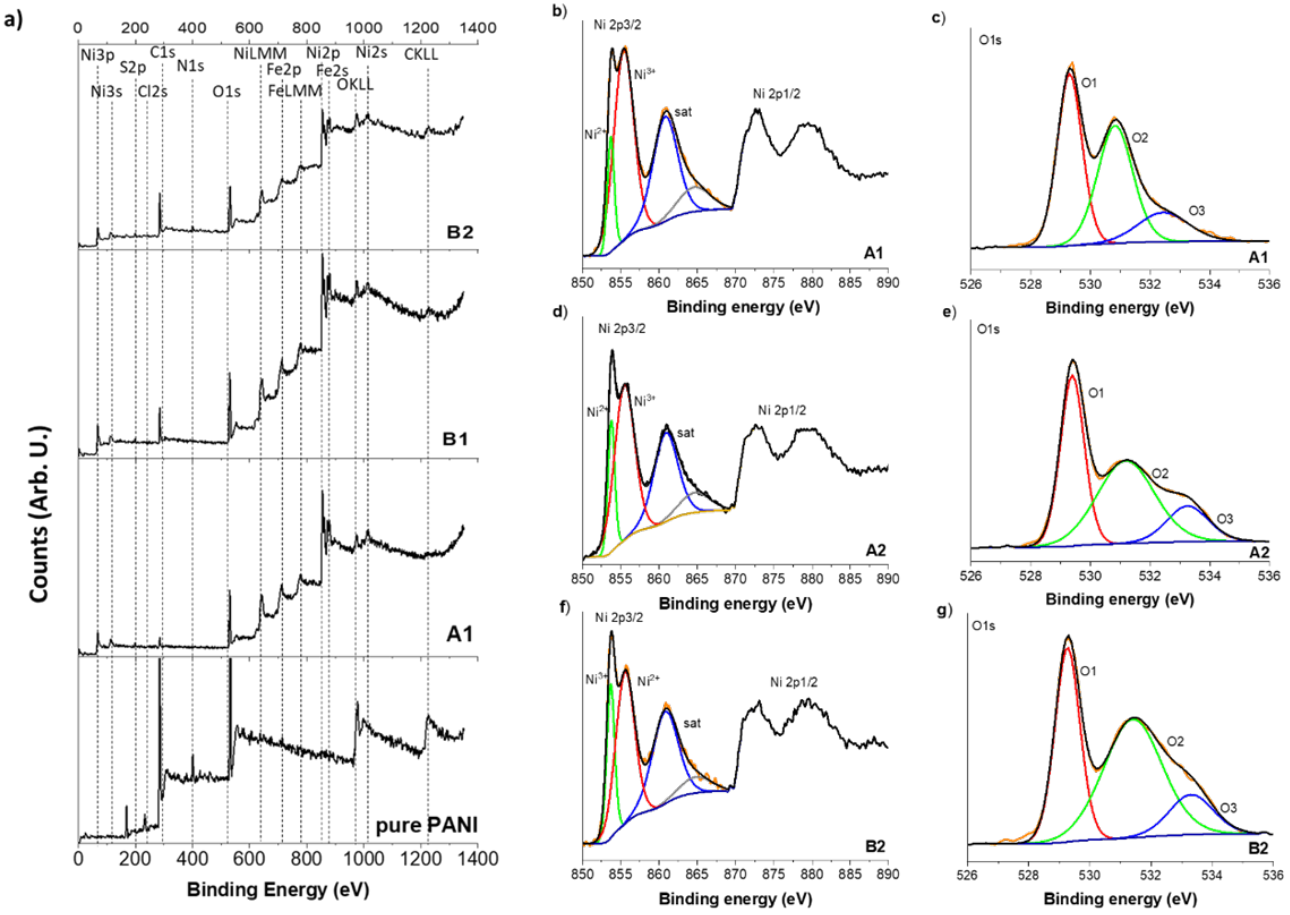

Figure 5. XPS spectra of bare PANI, pure NiO (A1), wheat-peel-extract mediated NiO (A2), and their corresponding composite of A2 with PANI, (**a**) Wide scan survey, (**b**,**c**) Ni2p3/2 and O1s of pure NiO (A1), (**d**,**e**) Ni2p3/2 and O1s of wheat-peel-extract mediated NiO (A2), (**f**,**g**) Ni2p3/2 and O1s of composite of B2 with PANI.

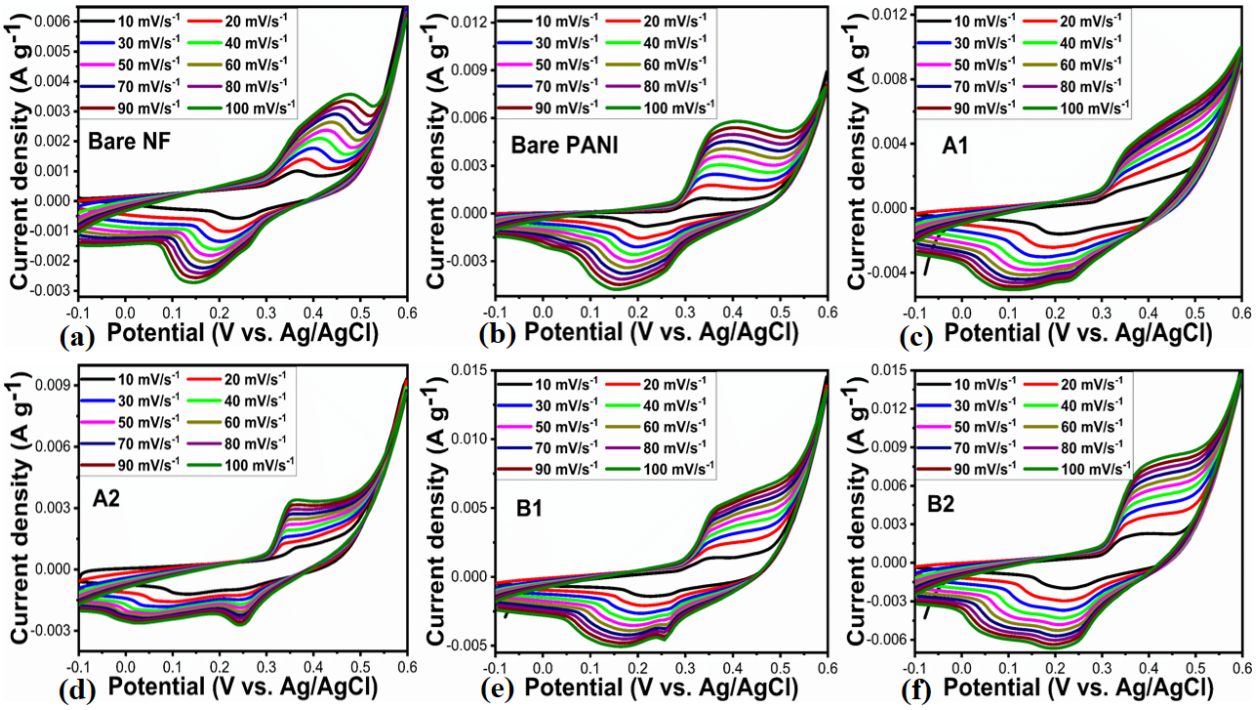

Figure 6. (**a**–**f**) CV curves of bare nickel foam and bare PANI, pure NiO (A1), wheat-peel-extract mediated NiO (A2) and their corresponding composites with PANI B1 and B2 respectively, at various scan rate in 3 M KOH electrolytic solution.

As shown in Figure 7a–f, galvanic charge-discharge (GCD) profiles of the electrode materials are presented, including bare nickel foam and PANI, A1, A2, and B1, B2 at different current densities (2, 3, 4, 5, and 10 Ag^{-1}). Based on the GCD profiles in Figure 7a–f, it can be concluded that GCD curves exhibit nonlinear behavior due to similar redox properties to CV curves [49]. Clearly, the PANI-based electrodes showed pseudocapacitance characteristics. For the purposes of demonstrating symmetric charge/discharge characteristics, each electrode material was tested at current densities between 2 Ag^{-1} and 10 Ag^{-1}. The presented electrode materials demonstrated significant variation in charge/discharge times at similar current densities, which confirms that specific capacitances vary. Based on the reported work [49], we calculated the specific capacitance of the proposed electrode materials at various current densities. Figure 8 shows the results of this calculation. Using a fixed current density of 2 Ag^{-1}, the GCD curves demonstrated that the B2 composite electrode had a higher specific capacitance of 1655.78 F/g than other proposed electrode materials. The specific capacitances of the electrode materials at various current densities are summarized in Supplementary Table S1. With increasing current density, it is evident that the specific capacitance decreases. There are several reasons why the B2 composite electrode has a higher specific capacitance, including the large surface area of 0.5 mL wheat peel extract-mediated NiO, the reduced optical band gap, which improves NiO's charge transfer kinetics, and the increased biocompatibility of NiO with polyaniline. Combining 0.5 mL wheat-peel-extract mediated NiO with polyaniline nanostructures provided unique interfacial redox properties, resulting in superior pseudocapacitance for the B2 composite.

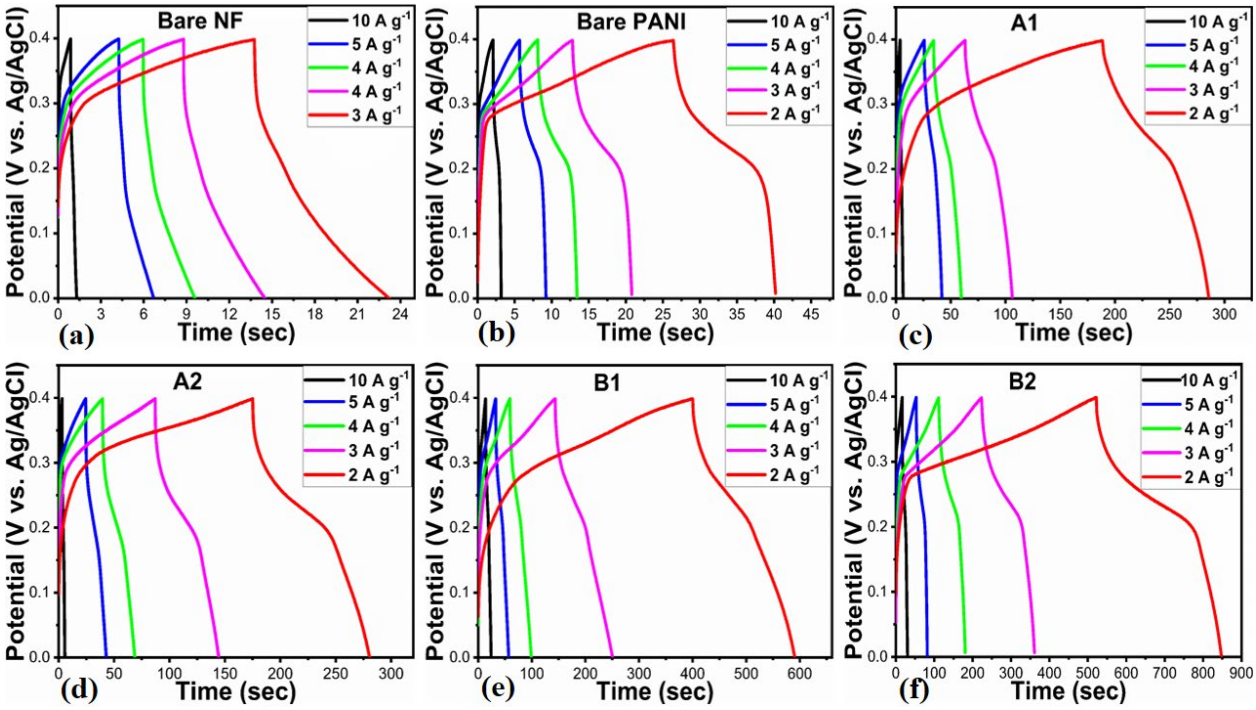

Figure 7. (**a**–**f**) GCD profiles of bare nickel foam and bare PANI, pure NiO (A1), wheat-peel-extract mediated NiO (A2), and their corresponding composites with PANI B1 and B2 respectively, at various current densities in 3 M KOH electrolytic solution.

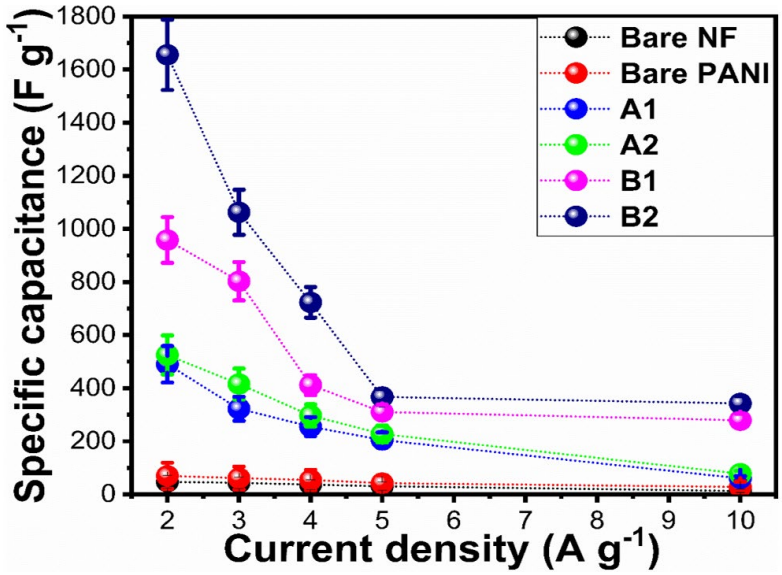

Figure 8. Calculated specific capacitance of bare nickel foam and bare PANI, pure NiO (A1), wheat-peel-extract mediated NiO (A2), and their corresponding composites with PANI B1 and B2 respectively, at various current densities in 3 M KOH electrolytic solution.

2.3. Asymmetric Supercapacitor Device Application of NiO/Polyaniline (B4) Composites

A significant potential exists for the integration of B2 composite materials into energy storage devices. As a result, asymmetric supercapacitors were constructed using rice husk-derived activated carbon (AC) as the cathode and the B2 composite as the anode in a 3 M KOH electrolytic solution. In Supplementary Figure S3, cyclic voltammetry (CV) curves of AC at different scan rates indicate that pseudocapacitor properties are negligible. Figure 9a shows CV measurements conducted in accordance with previous studies at various scan rates within a potential window of 0 to 1.6 V versus Ag/AgCl. During this potential

range, the oxidation and reduction peak positions were nearly identical at 1.6 V, indicating improved capacitance performance of the proposed asymmetric supercapacitor (ASC). The scan rates ranged from 10 mV/s to 150 mV/s within the 0 to 1.6 V potential window, as illustrated in Figure 9a. Due to the electrostatic interaction between NiO and PANI, the redox process of polyaniline (PANI) exhibited a rectangular shape with increasing scan rate, while the redox process remained unaffected by 100 mV/s scan rate in the proposed ASC device. In Figure 9b, galvanostatic charge-discharge (GCD) experiments conducted at various current densities demonstrate the energy storage performance of the proposed ASC device [50] provides an equation that can be used for estimating the specific capacitance:

$$C = I \times \Delta t / \Delta V \times m \quad (1)$$

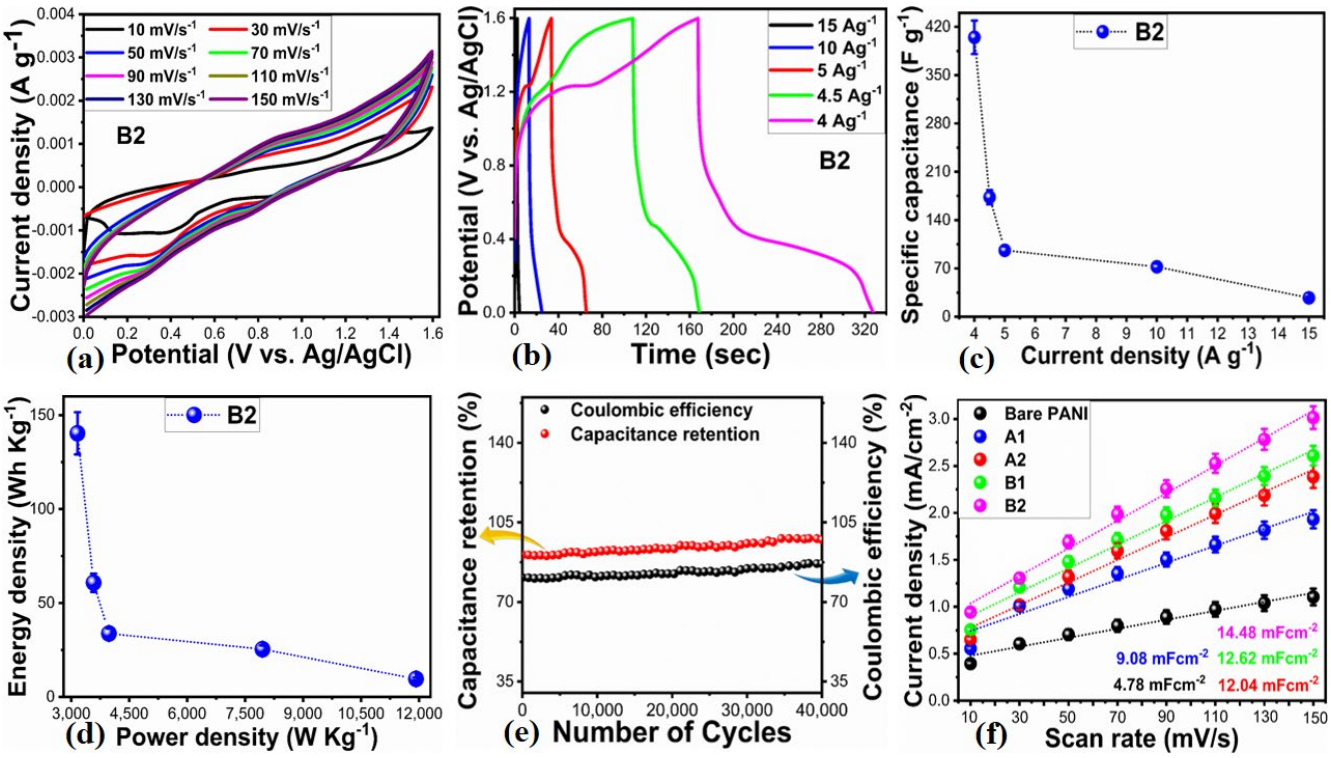

Figure 9. (**a**) CV curves of wheat-peel-extract mediated NiO (A2) and its composites with PANI (B2) at various scan rates in 3 M KOH electrolytic solution for demonstration of ASC device, (**b**) GCD curves of B2 in configured ASC device at different current densities, (**c**) calculated specific capacitance, (**d**) estimated energy density and power density, (**e**) capacitance retention % and columbic efficiency, (**f**) ECSA calculations of bare PANI, pure NiO (A1), wheat-peel-extract mediated NiO (A2) and their corresponding composites with PANI B1 and B2 respectively, at various scan rates in 3 M KOH electrolytic solution.

Here, C describes the specific capacitance, I is the discharge current, Δt is the discharge time, ΔV is voltage difference, and m is the active mass of electrode material.

Based on the specific capacitance measured at a fixed current density of 4 Ag^{-1}, the ASC device was found to have a specific capacitance of 404.8 Fg^{-1}. Based on Figure 9c, it was observed that varying the current density reduced the specific capacitance. In Figure 9d, the Ragone plot describes the energy and power density of the B composite electrode material. Energy density and power density were calculated using Equations (2) and (3).

$$E = [C \times (\Delta V)^2]/7.2 \quad (2)$$

$$P = [E \times (\Delta t)]/3.6 \quad (3)$$

Herein, E is energy density, P as power density, C is the specific areal capacitance, Δt is discharging time, and Δt is the voltage, defining the terms used in Equations (2) and (3), respectively.

In this study, the ASC device exhibited an energy density of 140.26 $Whkg^{-1}$ and a power density of 3166 Wkg^{-1} at a fixed current density of 4 Ag^{-1}. Compared to previous studies utilizing PANI electrode materials [51–55], these energy and power density values indicate a significant advancement in PANI-based electrode materials for potential commercial applications. Moreover, the cycling capability of the ASC device was evaluated over 40,000 GCD cycles at a fixed current density of 4 Ag^{-1}. As a result of these tests, the device demonstrated a capacitance retention of 97.9% and a columbic efficiency of 86.9%, illustrating its speedy charge transfer rate and suitability as an electrode material for supercapacitors, as shown in Figure 9e. Table 1 presents detailed performance metrics for the ASC device, and Supplementary Table S2 compares its performance with that of B2 as an anode material. In addition to being straightforward to synthesize, the electrode exhibits excellent energy storage performance and is cost-effective, making it a viable alternative for use in commercial applications. The Cdl values in Figure 9f are derived from the slope of the linear fit of the difference between anodic and cathodic side currents of CV curves at sweeping scan rates, divided by 2. Among PANI materials, the Cdl values were 4.78 $mFcm^{-2}$ in the bare PANI, 9.08 $mFcm^{-2}$ in the A1, 12.04 $mFcm^{-2}$ in the A2, 12.62 $mFcm^{-2}$ in the B1, and 14.48 $mFcm^{-2}$ in the B2, respectively. The corresponding CV curves used for the estimation of Cdl at various scan rates are shown in Supplementary Figure S4.

Table 1. Summary of obtained performance of ASC device on NiO/PANI composite (B2).

Material	Specific Capacitance (Fg^{-1})	Current Density (Ag^{-1})	Energy Density (Wh kg^{-1})	Power Density (W kg^{-1})	Columbic Efficiency %	Capacitance Retention (%)
B2	404.81	4	140.36	3160.00	86.9%	97.9
	173.21	4.5	60.82	3577.50		
	96.23	5	33.79	3975.00		
	72.33	10	25.40	7950.00		
	27.36	15	9.61	11,925.00		

2.4. Oxygen Evolution Reaction Performance of Wheat-Peel-Extract Mediated NiO@PANI Composites

OER demonstration is critical for applications related to energy storage, fuel cells, and hydrogen production. We studied various electrocatalysts, including bare PANI, bare nickel foam, pure NiO (A1), 0.5 mL of wheat-peel-extract mediated NiO (A2), and their composites with PANI, such as B1 and B2. The proposed electrocatalytic materials were evaluated by linear sweep voltammetry (LSV) using 1 M KOH electrolytic solution at a scan rate of 2 mV/s. Figure 10a illustrates that the OER activity of PANI and bare nickel foam was found to be negligible. Figure 10a presents the corresponding LSV curves without iR correction. For the bare PANI material, A1 and A2, and their composites with PANI, including B1 and B2, the overpotential values were found to be 420 mV, 390 mV, 370 mV, and 320 mV at 10 mA/cm^2, respectively. Among these, the B2 composite exhibited outstanding OER activity at relatively low overpotential, suggesting improved catalytic activity as a result of modified NiO surface, reduced optical band gap, increased active surface area, and improved electrical conductivity and redox properties through the combination of PANI.

As shown in Figure 10b, the overpotential of each electrocatalyst is displayed in bar graphs to provide a quick overview of its OER activity. Based on the Tafel equation, Figure 10c illustrates the OER kinetics for the electrocatalysts proposed. By analyzing the Tafel slope associated with each electrocatalyst, we are able to gain a deeper understanding of the material's role in the OER process reaction rate. By evaluating the Tafel slope, we are able to determine the exchange current density, which significantly facilitates the quantification of the inherent catalytic properties exhibited by various electrocatalysts. According to Figure 10c, the calculated Tafel slopes for bare PANI, A1, A2, and their composites with PANI, including B1 and B2, were 126 mV/dec, 92 mV/dec, 46 mV/dec, and 34 mV/dec, respectively. Compared to the other electrocatalysts, the B2 composite had a lower Tafel slope, suggesting a rapid electron transfer rate that was responsible for enhancing the adsorption rate of OH- at the electrode–electrolyte interface. Further, the low overpotential and Tafel slope for B2 composites indicate that the reaction kinetics proceed relatively faster in 1 M KOH electrolytic solution.

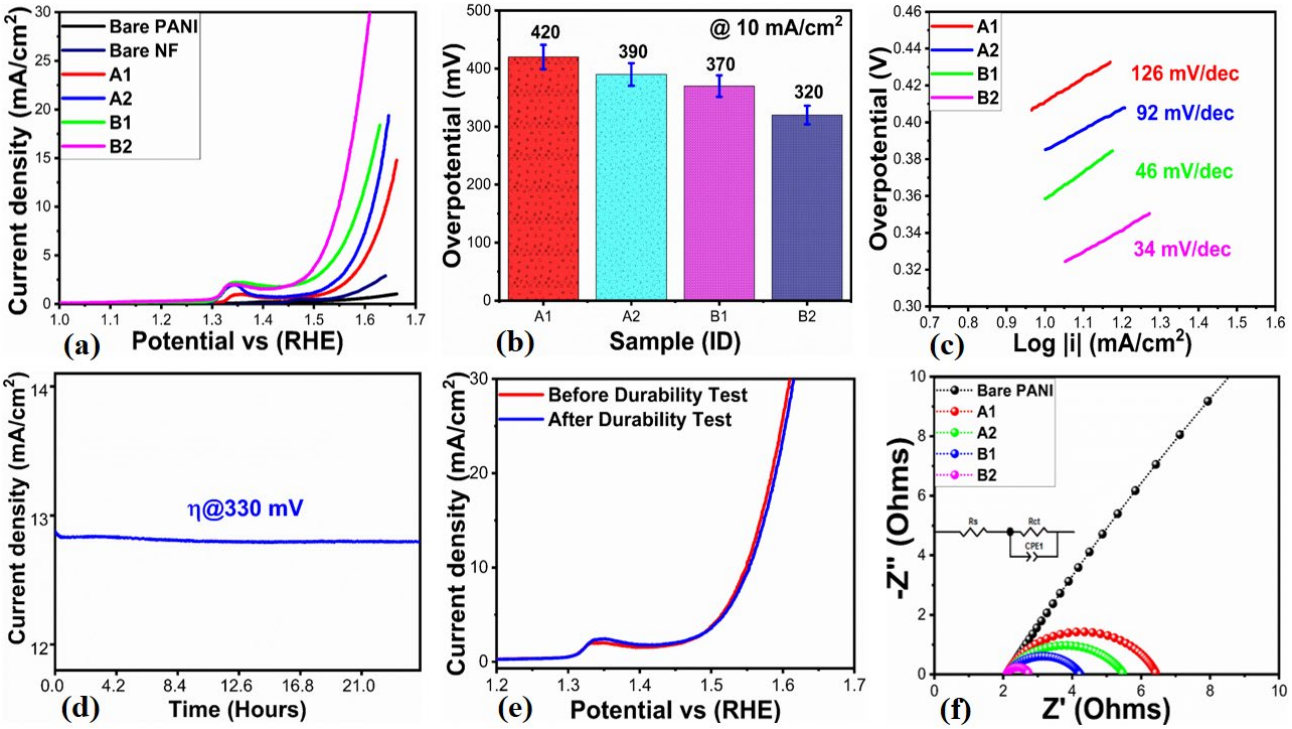

Figure 10. (**a**) LSV curves at 2 mV/s for the illustration of OER activity of bare nickel foam (NF), bare PANI, pure NiO (A1), wheat-peel-extract mediated NiO (A2), and their corresponding composites with PANI B1 and B2 respectively, in 1 M KOH electrolytic solution, (**b**) Bar graph description for overpotential, (**c**) Tafel slope analysis, (**d**) Chronoamperometry test for durability, (**e**) LSV curves for stability exploration through LSV curves before and after durability test at 2 mV/s, (**f**) Nyquist plots of bare PANI, A1, A2, and B1, B2 materials derived from EIS data.

According to Figure 10d, chronoamperometry was used to study the electrocatalytic stability of B2 composite material at a fixed overpotential of 330 mV for 30 h. The current density of the B2 composite was not affected by passage of time, indicating its high durability. According to the chronoamperometry test, the strong durability of NiO can be attributed to its modified surface by wheat peel extract, which showed high compatibility with PANI. Figure 10e shows the LSV curves measured before and after the durability test that confirm the stability. OER's onset potential remained unchanged, and the overpotential of the B4 composite electrocatalyst was retained, confirming the material's high stability. In previous publications, it has been noted that PANI is very stable in alkaline media. In

order to investigate the charge transport properties of the synthesized electrocatalysts, electrochemical impedance spectroscopy (EIS) was employed. EIS measurements were conducted under the following conditions: a frequency range of 100 kHz to 0.1 Hz, an amplitude of 10 mV, and an OER onset potential as the applied potential in 1 M KOH electrolytic solution. As shown in Figure 10f, bare PANI, A1, A2, and their composites with PANI, including B1 and B2, were simulated using z-view software version 3.20. A semi-circular shape was observed in the Nyquist plots. In the inset of Figure 10f, the equivalent circuit is shown with elements such as solution resistance (Rs), charge transfer resistance (Rct), and double-layer capacitance (Cdl). According to the EIS fitting, the charge transfer resistance of bare PANI, A1, A2, and their composites with PANI, including B1 and B2, was estimated to be 142.3, 4.3, 3.4, 2.1, and 0.6 Ohms, respectively. According to these Rct values, the electrochemical activity of the B2 composite is superior to the other materials due to its lowest charge transfer resistance. B2 composite material has an enhanced charge transfer kinetics due to the modified surface, the reduced optical band gap in PANI, as well as the synergistic effect between NiO and PANI. According to the EIS study, the improved electrochemical performance of B2 composite material can be attributed to its fast charge transfer rate and increased electroactive surface area, demonstrating excellent energy storage and conversion capabilities. In Supplementary Table S3, the results for the B2 composite regarding OER are compared with recent electrocatalytic materials. Compared to previously developed materials, the presented system is simple and eco-friendly, providing enhanced OER activity.

3. Experimental Section

3.1. Chemicals

Aniline, concentrated hydrochloric acid, sulfuric acid, potassium persulfate, ethanol, potassium hydroxide, nickel foam, Nafion (5%), nickel chloride hexahydrate, and 30% aqueous ammonia solution were used as solvents without further distillation or crystallization. These chemicals were provided by Sigma Aldrich Karachi, Sindh Pakistan. The wheat peel was purchased from a local market in the district Jamshoro, Sindh Pakistan.

3.2. Synthesis of NiO/PANI Composites Using Hydrothermal and Chemical Oxidation Polymerization

The NiO and PANI composites were prepared by dissolving 250 g of wheat peel extract in 300 mL of deionized water and heating at 70 °C for three hours. Once the filtrate had been collected, it was stored at 4 °C in a refrigerator when not in use. Using the hydrothermal method, NiO was synthesized with and without wheat peel extract at 95 °C for five hours, followed by thermal calcination at 500 °C for 5 h. An earlier study reported a calcination temperature of 500 °C [3]. At this temperature, the nickel hydroxide phase is completely transformed into nickel oxide. A typical hydrothermal process using 0.1 M nickel chloride hexahydrate and 5 mL of aqueous ammonia was conducted with the sample designated as (A1). A thick aluminum sheet was then placed over the growth solution and placed in an electric oven. Under the conditions described in the previous paragraph, NiO was obtained in its pure phase by calcination. During the synthesis of NiO, cellulose and starch were used as reducing agents, and protein from wheat peel extract was used as a structure-directing agent. These phytochemicals played a significant role in altering the growth kinetics of the nickel hydroxide crystals, which resulted in significant changes to their size and shape. Consequently, wheat peel extract was used to prepare NiO nanostructures. In order to prepare surface-modified NiO, 0.5 mL and 1 mL of wheat peel extract were used under the same hydrothermal and calcination conditions and labelled as (A2) and (A3), respectively. A chemical oxidation polymerization method was then used to synthesize NiO/PANI composites. A bare PANI was prepared by chemical oxidation polymerization under the

following conditions: 0.1 M aniline was dissolved in concentrated HCl in one beaker and 0.1 M potassium persulfate in another beaker. Dropwise additions of potassium persulfate solution were then made to the aniline solution, and the solution was left undisturbed for 6 h. Following the collection of PANI particles on filter paper, the sample was washed several times with deionized water, ethanol, and acetone to remove any unwanted residues. NiO materials, including A1, A2, and A3, weighing 0.3 g, were added to three separate beakers containing 0.1 M aniline solution, followed by 0.1 M potassium persulfate. The samples were subsequently labeled as B1, B2, and B3, representing NiO/PANI composites.

3.3. Characterization

The structure, morphology, functional groups, surface chemical composition, and optical properties of the synthesized materials have been investigated using a comprehensive array of analytical techniques. Scanning electron microscopy (SEM) was performed by means of a Zeiss GeminiSEM 500 scanning electron microscope equipped with a field emission gun at an accelerating voltage of 2 kV. Under experimental conditions on the Rigaku Ultima IV 8 X-ray diffractometer, with a range of 10° to 80°, a current of 40 mA, and a voltage of 40 kV, X-ray diffraction (XRD) was used to determine the phase and purity of the samples. To analyze functional groups and chemical structure, the Nicolet iS10 Fourier transform infrared spectrometer (FTIR) was used. Optical band gap measurements were conducted using a UV-visible spectrometer. An ultrasonic bath is used to dissolve 0.002 to 0.003 g of NiO in deionised water. After the particles have been dispersed and centrifuged, the dispersed slurry has been collected and used to record the UV-visible absorption spectrum. In order to investigate the chemical composition of the surface, X-ray photoelectron spectroscopy (XPS) was used.

3.4. Electrochemical Characterization

An active electrode material weighing 0.005 g was immersed in a solution composed of deionized water and ethanol containing 3 mL. A subsequent addition of 50 µL of 5% Nafion was added, and the mixture was sonicated for 20 min in an ultrasonic bath. Alumina paste and silicon paper were used to clean the glassy carbon electrode (GCE), followed by washing with deionized water and ethanol. A 2×2 cm^2 piece of nickel foam was also washed with a concentrated HCl solution and deionized water. The GCE was then decorated with 5 µL of active electrode material ink and dried with an air blower. Using the dip coating method, the active material was deposited on the cleaned nickel foam piece, repeated six times, and sintered for 25 min at 65 °C. Nickel foam as well as modified GCE were utilized as working electrodes. The loading mass of electrode material was approximately 0.2 mg. For the evaluation of the electrochemical properties of the synthesized electrode materials, a variety of electrochemical techniques were employed, including linear sweep voltammetry (LSV), cyclic voltammetry (CV), electrochemical impedance spectroscopy (EIS), chronoamperometry, and galvanic charge-discharge (GCD). The EIS was conducted between 100 kHz and 0.1 Hz in frequency, with an amplitude of 10 mV and a biasing potential of the OER onset potential in 1 M KOH. To characterize OER, a 2 mV/s LSV was conducted in a 1 M KOH electrolytic solution. An assessment of the pseudocapacitance properties of the prepared electrode materials in a 3 M KOH solution was performed using CV and GCD. Due to the high adsorption of electrolytic ions on KOH, the high concentration of KOH was used in order to increase the observation of the charge storage capacity of the electrode materials.

4. Conclusions

The chemical oxidation polymerization process was used to prepare PANI composites containing reduced optical band gap NiO nanostructures. A study of the structure, surface chemical composition, optical band gap, and functional group analysis was conducted. NiO/PANI prepared with 0.5 mL of wheat peel extract was found to be highly efficient for improving asymmetric supercapacitor (ASC) and oxygen evolution reactions in KOH electrolytic solution. A NiO/PANI composite was found to have an OER activity at an overpotential of 320 mV at 10 mA/cm^2. Due to its enhanced pseudocapacitance, NiO/PANI composite was applied to the development of an asymmetric supercapacitor device. At a fixed current density of 4 A/g, the ASC device demonstrated a high energy density of 140 $Whkg^{-1}$, a high-power density of 3160 Wkg^{-1}, and a high specific capacitance of 404 Fg^{-1}. During repeatable GCD cycles of 40,000 at a current density of 4 Ag^{-1}, an outstanding capacitance of almost 97.9% and columbic efficiency of 86.9% were observed, which confirms the electrode's superior cycling stability.

Supplementary Materials: The following supporting information can be downloaded at: https://www.mdpi.com/article/10.3390/catal15060508/s1, Figure S1: Tauc's plots of bare PANI, A1, A2, B1, and B2 for the estimation of optical band gap. Figure S2: XPS survey spectra of Pure PANI, pure NiO (A1), and A2 and B2 composites; Figure S3: CV curves at different scan rates. Activated carbon in 3 M KOH solution; Figure S4: (a–e) CV curves in non-faradic region of bare PANI, A1, A2, and B1 and B2 materials at various scan rates in 3 M KOH electrolytic solution for the estimation of ECSA values; Table S1. Summarized electrochemical performance of various electrode materials such as bare nickel foam/PANI, A1, A2, and B2, B2; Table S2: Comparative study of B2 as anode material for ASC with recently reported ASC device; Table S3: Comparative study of B2 as OER electrocatalytic material with recently reported ASC devices. References [56–72] are cited in the Supplementary Materials.

Author Contributions: F.H., material synthesis and partial electrochemical tests; W.D., partial material characterization; R.K., partial electrochemical tests and material synthesis; J.P., involved in FTIR measurements; G.D., optical studies; A.R., EIS analysis; H.K., partial electrochemical tests; R.M., optical band gap analysis; M.A.B. (Masroor Ali Bhellar), partial material characterization; A.M., partial electrochemical measurements; K.A., partial structural studies; A.T., XRD analysis and wrote first draft; M.A.B. (Muhammad Ali Bhatti), supervised overall electrochemical tests; E.D., validated results and edited final draft; R.M.I., visualized results and edited final draft; B.V., SEM analysis and wrote first draft; Z.H.I., main supervision and wrote first draft. All authors have read and agreed to the published version of the manuscript.

Funding: This research was funded by Pakistan Science Foundation and Natural Science Foundation China for partially supporting the project PSF-NSFC/202307/427. They would also like to acknowledge the partial support of Ajman University, Internal Research Grant No. [DGSR Ref: 2024-IRG-HBS-01]. B.V. would like to thank the platform "Microscopies, Microprobes and Metallography (3M)" (Institut Jean Lamour, IJL, Nancy, France).

Institutional Review Board Statement: Not applicable.

Informed Consent Statement: Not applicable.

Data Availability Statement: Data sets generated during the current study are available from the corresponding author on reasonable request.

Conflicts of Interest: The authors declare no conflicts of interest in the presented research work.

References

1. Chen, G.Z. Supercapacitor and supercapattery as emerging electrochemical energy stores. *Int. Mater. Rev.* **2017**, *62*, 173–202. [CrossRef]
2. Krishnasamy, K.; Purushothaman, K.K. Preparation and characterisation of MnS@ Mn_3O_4/C nanoflakes for hybrid supercapacitor applications. *Mater. Technol.* **2022**, *37*, 63–70. [CrossRef]
3. Chatterjee, S.; Ray, A.; Mandal, M.; Das, S.; Bhattacharya, S.K. Synthesis and characterization of CuO-NiO nanocomposites for electrochemical supercapacitors. *J. Mater. Eng. Perform.* **2020**, *29*, 8036–8048. [CrossRef]
4. Sidhu, N.K.; Rastogi, A.C. Vertically aligned ZnO nanorod core-polypyrrole conducting polymer sheath and nanotube arrays for electrochemical supercapacitor energy storage. *Nanoscale Res. Lett.* **2014**, *9*, 453. [CrossRef]
5. Nuamah, R.A.; Noormohammed, S.; Sarkar, D.K. Pulsed reverse potential electrodeposition of carbon-free Ni/Nio nanocomposite thin film electrode for energy storage supercapacitor electrodes. *Coatings* **2021**, *11*, 780. [CrossRef]
6. Kumar, R.; Abdel-Galeil, M.M.; Matsuda, A.; Moshkalev, S.A. One step synthesis Pd/NiO@ rGO/CNTs nanocomposite for energy storage as supercapacitor application. In *Journal of Physics: Conference Series*; IOP Publishing: Bristol, UK, 2020; Volume 1461, p. 012109.
7. Nguyen, T.V.; Nguyen, T.D.; Pham, N.V.; Nguyen, T.A. Ta DV Monodisperse and size-tunable high-quality factor microsphere biolasers. *Opt. Lett.* **2021**, *46*, 2517–2520. [CrossRef]
8. Shi, H.H.; Naguib, H.E. Fabrication and characterization of polyaniline-graphene nanoplatelets composite electrode materials for hybrid supercapacitor applications. In *Behavior and Mechanics of Multifunctional Materials and Composites*; SPIE: Bellingham, WA, USA, 2015; Volume 9432, pp. 189–197.
9. Payami, E.; Teimuri-Mofrad, R. A novel ternary Fe_3O_4@ Fc-GO/PANI nanocomposite for outstanding supercapacitor performance. *Electrochim. Acta* **2021**, *383*, 138296. [CrossRef]
10. Sookhakian, M.; Basirun, W.J.; Teridi, M.A.; Mahmoudian, M.R.; Azarang, M.; Zalnezhad, E.; Yoon, G.H.; Alias, Y. Prussian blue-nitrogen-doped graphene nanocomposite as hybrid electrode for energy storage applications. *Electrochim. Acta* **2017**, *230*, 316–323. [CrossRef]
11. Aljaafari, A.; Parveen, N.; Ahmad, F.; Alam, M.W.; Ansari, S.A. Self-assembled cube-like copper oxide derived from a metal-organic framework as a high-performance electrochemical supercapacitive electrode material. *Sci. Rep.* **2019**, *9*, 9140. [CrossRef]
12. Çıplak, Z.; Yıldız, A.; Yıldız, N. Green preparation of ternary reduced graphene oxide-au@ polyaniline nanocomposite for supercapacitor application. *J. Energy Storage* **2020**, *32*, 101846. [CrossRef]
13. Kanaujiya, N.; Kumar, N.; Singh, M.; Sharma, Y.; Varma, G.D. $CoMn_2O_4$ nanoparticles decorated on 2D MoS2 frame: A synergetic energy storage composite material for practical supercapacitor applications. *J. Energy Storage* **2021**, *35*, 102302. [CrossRef]
14. Tuichai, W.; Karaphun, A.; Ruttanapun, C. Ag nanomaterials deposited reduced graphene oxide nanocomposite as an advanced hybrid electrode material for asymmetric supercapacitor device. *J. Alloys Compd.* **2020**, *849*, 156516. [CrossRef]
15. Li, C.K.; Lin, L.; Xiong, S.L.; Ge, M.Y.; Li, X.B.; Li, T.P.; Lu, F.J.; Zhang, S.N.; Tuo, Y.L.; Nang, Y.; et al. HXMT identification of a non-thermal X-ray burst from SGR J1935+ 2154 and with FRB 200428. *Nat. Astron.* **2021**, *5*, 378–384. [CrossRef]
16. Kalusulingam, R.; Ravi, K.; Mathi, S.; Mikhailova, T.S.; Srinivasan, K.; Biradar, A.V.; Myasoedova, T.N. Bagasse derived N-doped graphitic carbon encapsulated cobalt nanoparticles as an efficient bifunctional catalyst for water splitting reactions. *Colloids Surf. A Physicochem. Eng. Asp.* **2024**, *692*, 133959. [CrossRef]
17. Bhadu, G.R.; Parmar, B.; Patel, P.; Paul, A.; Chaudhari, J.C.; Srivastava, D.N.; Suresh, E. Co@ N-doped carbon nanomaterial derived by simple pyrolysis of mixed-ligand MOF as an active and stable oxygen evolution electrocatalyst. *Appl. Surf. Sci.* **2020**, *529*, 147081. [CrossRef]
18. Jamesh, M.I.; Harb, M. Tuning the electronic structure of the earth-abundant electrocatalysts for oxygen evolution reaction (OER) to achieve efficient alkaline water splitting—A review. *J. Energy Chem.* **2021**, *56*, 299–342. [CrossRef]
19. Li, J.; Du, X.; Zhang, X. Controlled synthesis of $NiWO_4$ combined with $NiSe_2$ with heterostructure on nickel foam for efficient overall water splitting. *J. Alloys Compd.* **2023**, *951*, 169941. [CrossRef]
20. Zhong, X.; Shu, C.; Su, X.; Wang, W.; Gong, J. Insight into improved oxygen evolution reaction on electronic modulation of phosphorus doped $NiCo_2O_4$. *Mater. Today Commun.* **2022**, *31*, 103708. [CrossRef]
21. Patel, K.B.; Parmar, B.; Ravi, K.; Patidar, R.; Chaudhari, J.C.; Srivastava, D.N.; Bhadu, G.R. Metal-organic framework derived core-shell nanoparticles as high performance bifunctional electrocatalysts for HER and OER. *Appl. Surf. Sci.* **2023**, *616*, 156499. [CrossRef]
22. Özhava, D.; Özkar, S. Nanoceria supported rhodium (0) nanoparticles as catalyst for hydrogen generation from methanolysis of ammonia borane. *Appl. Catal. B Environ.* **2018**, *237*, 1012–1020. [CrossRef]
23. Aneggi, E.; de Leitenburg, C.; Trovarelli, A. Influence of nanoscale surface arrangements on the oxygen transfer ability of ceria–zirconia mixed oxide. *Inorganics* **2020**, *8*, 34. [CrossRef]
24. Liu, Z.; Li, N.; Zhao, H.; Zhang, Y.; Huang, Y.; Yin, Z.; Du, Y. Regulating the active species of $Ni(OH)_2$ using CeO_2: 3D CeO_2/$Ni(OH)_2$/carbon foam as an efficient electrode for the oxygen evolution reaction. *Chem. Sci.* **2017**, *8*, 3211–3217. [CrossRef]

25. Flores-Melo, L.M.; Arce-Estrada, E.; Trujillo-Olivares, I.; Sandoval-Pineda, J.M.; Reyes-Rodríguez, J.L.; de Guadalupe González-Huerta, R. Influence of CeO_2 nanoparticles in the stability of electrodeposited Ni anodes for alkaline electrolysers. *Int. J. Hydrogen Energy* **2023**, *48*, 18141–18153. [CrossRef]
26. Rui, N.; Zhang, X.; Zhang, F.; Liu, Z.; Cao, X.; Xie, Z.; Zou, R.; Senanayake, S.D.; Yang, Y.; Rodriguez, J.A.; et al. Highly active Ni/CeO_2 catalyst for CO_2 methanation: Preparation and characterization. *Appl. Catal. B Environ.* **2021**, *282*, 119581. [CrossRef]
27. Tao, Y.; Gong, F.H.; Wang, H.; Wu, H.P.; Tao, G.L. Microwave-assisted preparation of cerium dioxide nanocubes. *Mater. Chem. Phys.* **2008**, *112*, 973–976. [CrossRef]
28. Saha, E.; Bhadu, G.R.; Mitra, J. Ni (II) supramolecular gel-derived Ni (0) nanoclusters decorated with optimal N, O-doped graphitized carbon as bifunctional electrocatalysts for oxygen and hydrogen evolution reactions. *Int. J. Hydrogen Energy* **2023**, *48*, 8115–8126. [CrossRef]
29. Okafor, O.B.; Popoola, A.P.; Popoola, O.M.; Adeosun, S.O. Review on the recent development on polyaniline and transition metal oxides composite electrode for supercapacitor application. *Next Mater.* **2025**, *6*, 100389. [CrossRef]
30. Patel, K.B.; Mariyaselvakumar, M.; Vyas, G.; Chaudhari, J.C.; Patidar, R.; Srinivasan, K.; Srivastava, D.N.; Bhadu, G.R. Nickel oxide doped ceria nanoparticles ($NiO@CeO_2$) for boosting oxygen evolution reaction and enhancing stability. *Appl. Surf. Sci.* **2024**, *649*, 159212. [CrossRef]
31. Deraz, N.M. Effect of NiO content on structural, surface and catalytic characteristics of nano-crystalline NiO/CeO_2 system. *Ceram. Int.* **2012**, *38*, 747–753. [CrossRef]
32. Kotomin, E.A.; Eglitis, R.I.; Popov, A.I. Charge distribution and optical properties of and F centres in crystals. *J. Phys. Condens. Matter* **1997**, *9*, L315. [CrossRef]
33. Janotti, A.; Van de Walle, C.G. Oxygen vacancies in ZnO. *Appl. Phys. Lett.* **2005**, *87*, 122102. [CrossRef]
34. Muñoz Ramo, D.; Gavartin, J.L.; Shluger, A.L.; Bersuker, G. Spectroscopic properties of oxygen vacancies in monoclinic HfO_2 calculated with periodic and embedded cluster density functional theory. *Phys. Rev. B—Condens. Matter Mater. Phys.* **2007**, *75*, 205336. [CrossRef]
35. Chen, H.; Yang, S. Methods and strategies for achieving high-performance carbon-based perovskite solar cells without hole transport materials. *J. Mater. Chem. A* **2019**, *7*, 15476–15490. [CrossRef]
36. Du, Y.; Zhang, X.; Shi, Y.; Hou, X.; Li, F.; Zhang, Q.; Tai, Q.; Liu, P.; Zhao, X.Z. Optimized crystallization and defect passivation with Yttrium (III) doped MAPbBr3 film for highly efficient and stable hole-transport-layer-free carbon-based perovskite solar cells. *J. Alloys Compd.* **2022**, *890*, 161909. [CrossRef]
37. Chen, X.; Zhang, F.; Yang, Z.; Huang, S. One-pot hydrothermal synthesis of reduced graphene oxide/carbon nanotube/α-$Ni(OH)_2$ composites for high performance electrochemical supercapacitor. *J. Power Sources* **2013**, *243*, 555–561. [CrossRef]
38. Azari-Hamidian, S.; Harbach, R.E. Arthropod-borne and arthropod-related viruses in Iran and neighboring countries. *Parazitologiâ* **2023**, *57*, 356–440. [CrossRef]
39. Poyyamozhi, N.; Kumar, S.S.; Kumar, R.A.; Soundararajan, G. An investigation into enhancing energy storage capacity of solar ponds integrated with nanoparticles through PCM coupling and RSM optimization. *Renew. Energy* **2024**, *221*, 119733. [CrossRef]
40. Ayad, M.; El-Hefnawy, G.; Zaghlol, S. Facile synthesis of polyaniline nanoparticles; its adsorption behavior. *Chem. Eng. J.* **2013**, *217*, 460–465. [CrossRef]
41. Keerthana, S.P.; Yuvakkumar, R.; Kumar, P.S.; Ravi, G.; Velauthapillai, D. Rare earth metal (Sm) doped zinc ferrite ($ZnFe_2O_4$) for improved photocatalytic elimination of toxic dye from aquatic system. *Environ. Res.* **2021**, *197*, 111047. [CrossRef]
42. Hassanien, A.S.; Akl, A.A. Effect of Se addition on optical and electrical properties of chalcogenide CdSSe thin films. *Superlattices Microstruct.* **2016**, *89*, 153–169. [CrossRef]
43. Sakamoto, K.; Hayashi, F.; Sato, K.; Hirano, M.; Ohtsu, N. XPS spectral analysis for a multiple oxide comprising NiO, TiO_2, and $NiTiO_3$. *Appl. Surf. Sci.* **2020**, *526*, 146729. [CrossRef]
44. Yang, J.; Yang, Z.; Meng, T.; Han, Y.; Wang, X.; Zhang, Q. Effects of silicon doping on the performance of tin oxide thin film transistors. *Phys. Status Solidi (A)* **2016**, *13*, 1010–1015. [CrossRef]
45. Liu, W.; Lu, C.; Wang, X.; Liang, K.; Tay, B.K. In situ fabrication of three-dimensional, ultrathin graphite/carbon nanotube/NiO composite as binder-free electrode for high-performance energy storage. *J. Mater. Chem. A* **2015**, *3*, 624–633. [CrossRef]
46. Myasoedova, T.N.; Grigoryev, M.N.; Mikhailova, T.S. Effect of nickel and manganese doping on the structure, morphology and the electrochemical performance of the silicon-carbon films. *J. Alloys Compd.* **2021**, *855*, 157504. [CrossRef]
47. Soudagar, N.M.; Pardeshi, A.R.; Padvi, M.A.; Pandit, V.K.; Joshi, S.S. The performance studies of polyaniline-functionalized carbon nanotube supercapacitor at room temperature. In *AIP Conference Proceedings*; AIP Publishing: Melville, NY, USA, 2024; Volume 3139.
48. Zhang, M.; Nautiyal, A.; Du, H.; Wei, Z.; Zhang, X.; Wang, R. Electropolymerization of polyaniline as high-performance binder free electrodes for flexible supercapacitor. *Electrochim. Acta* **2021**, *376*, 138037. [CrossRef]

49. Zhang, Y.S.; Lu, C.; Hu, Y.X.; Zhang, B.M.; Li, J.; Tian, C.Y.; Zhang, D.T.; Kong, L.B.; Liu, M.C. Assemble from 0D to 3D: Anchored 0D molybdenum carbide on 3D octahedral amorphous carbon with excellent capacitive properties. *J. Mater. Sci.* **2020**, *55*, 15562–15573. [CrossRef]
50. Han, L.; Cui, S.; Yu, H.Y.; Song, M.; Zhang, H.; Grishkewich, N.; Huang, C.; Kim, D.; Tam, K.M. Self-healable conductive nanocellulose nanocomposites for biocompatible electronic skin sensor systems. *ACS Appl. Mater. Interfaces* **2019**, *11*, 44642–44651. [CrossRef]
51. Zhu, Y.; Xu, H.; Chen, P.; Bao, Y.; Jiang, X.; Chen, Y. Electrochemical performance of polyaniline-coated γ-MnO2 on carbon cloth as flexible electrode for supercapacitor. *Electrochim. Acta* **2022**, *413*, 140146. [CrossRef]
52. Mao, N.; Chen, W.; Meng, J.; Li, Y.; Zhang, K.; Qin, X.; Zhang, H.; Zhang, C.; Qiu, Y.; Wang, S. Enhanced electrochemical properties of hierarchically sheath-core aligned carbon nanofibers coated carbon fiber yarn electrode-based supercapacitor via polyaniline nanowire array modification. *J. Power Sources* **2018**, *399*, 406–413. [CrossRef]
53. Li, K.; Liu, X.; Chen, S.; Pan, W.; Zhang, J. A flexible solid-state supercapacitor based on graphene/polyaniline paper electrodes. *J. Energy Chem.* **2019**, *32*, 166–173. [CrossRef]
54. Yang, X.; Qiu, Y.; Zhang, M.; Zhang, L.; Li, H. Facile fabrication of polyaniline/graphene composite fibers as electrodes for fiber-shaped supercapacitors. *Appl. Sci.* **2021**, *11*, 8690. [CrossRef]
55. Shao, F.; Niu, Y.; Li, B.; Li, G.; Yang, Z.; Su, Y.; Zhang, Y.; Hu, N. Binary nanosheet frameworks of graphene/polyaniline composite for high-areal flexible supercapacitors. *Mater. Chem. Phys.* **2021**, *273*, 125128. [CrossRef]
56. Zheng, X.; Ye, Y.; Yang, Q.; Geng, B.; Zhang, X. Ultrafine nickel–copper carbonate hydroxide hierarchical nanowire networks for high-performance supercapacitor electrodes. *Chem. Eng. J.* **2016**, *290*, 353–360. [CrossRef]
57. Ji, S.H.; Chodankar, N.R.; Kim, D.H. Aqueous asymmetric supercapacitor based on RuO_2-WO_3 electrodes. *Electrochim. Acta* **2019**, *325*, 134879. [CrossRef]
58. Wang, X.L.; Zhang, G.F.; Nasser, R.; Jiang, T.T.; Cao, Q.W.; Gong, M.Z.; Li, X.Y.; Song, J.M. Controllable synthesis of Co/Ni basic carbonate composite via regulating Co/Ni ratio with super rate performance for asymmetric solid-state supercapacitor. *J. Alloys Compd.* **2022**, *906*, 164270. [CrossRef]
59. Du, W.; Wang, X.; Zhan, J.; Sun, X.; Kang, L.; Jiang, F.; Zhang, X.; Shao, Q.; Dong, M.; Liu, H.; et al. Biological cell template synthesis of nitrogen-doped porous hollow carbon spheres/MnO_2 composites for high-performance asymmetric supercapacitors. *Electrochim. Acta* **2019**, *296*, 907–915. [CrossRef]
60. Zhu, D.; Sun, X.; Yu, J.; Liu, Q.; Liu, J.; Chen, R.; Zhang, H.; Li, R.; Yu, J.; Wang, J. Rationally designed $CuCo_2O_4$@$Ni(OH)_2$ with 3D hierarchical core-shell structure for flexible energy storage. *J. Colloid Interface Sci.* **2019**, *557*, 76–83. [CrossRef] [PubMed]
61. Zhang, M.; Liu, W.; Liang, R.; Tjandra, R.; Yu, A. Graphene quantum dot induced tunable growth of nanostructured $MnCo_2O_{4.5}$ composites for high-performance supercapacitors. *Sustain. Energy Fuels* **2019**, *3*, 2499–2508. [CrossRef]
62. Zhang, X.; Li, Z.; Yu, Z.; Wei, L.; Guo, X. Mesoporous NiMoO4 microspheres decorated by Ag quantum dots as cathode material for asymmetric supercapacitors: Enhanced interfacial conductivity and capacitive storage. *Appl. Surf. Sci.* **2020**, *505*, 144513. [CrossRef]
63. Ding, S.; Li, X.; Jiang, X.; Hu, Q.; Yan, Y.; Zheng, Q.; Lin, D. Core-shell nanostructured ZnO@ CoS arrays as advanced electrode materials for high-performance supercapacitors. *Electrochim. Acta* **2020**, *354*, 136711. [CrossRef]
64. Xuan, H.; Li, H.; Yang, J.; Liang, X.; Xie, Z.; Han, P.; Wu, Y. Rational design of hierarchical core-shell structured $CoMoO_4$@CoS composites on reduced graphene oxide for supercapacitors with enhanced electrochemical performance. *Int. J. Hydrogen Energy* **2020**, *45*, 6024–6035. [CrossRef]
65. Kumar, S.; Satpathy, B.K.; Pradhan, D. Morphology-controlled synthesis of a NiCo-carbonate layered double hydroxide as an electrode material for solid-state asymmetric supercapacitors. *Mater. Adv.* **2024**, *5*, 2271–2284. [CrossRef]
66. Liu, P.F.; Zhang, L.; Zheng, L.R.; Yang, H.G. Surface engineering of nickel selenide for an enhanced intrinsic overall water splitting ability. *Mater. Chem. Front.* **2018**, *2*, 1725–1731. [CrossRef]
67. Nagajyothi, P.C.; Ramaraghavulu, R.; Munirathnam, K.; Yoo, K.; Shim, J. One-pot hydrothermal synthesis: Enhanced MOR and OER performance using low-cost Mn_3O_4 electrocatalyst. *Int. J. Hydrogen Energy* **2021**, *46*, 13946–13951. [CrossRef]
68. He, J.; Wang, M.; Wang, W.; Miao, R.; Zhong, W.; Chen, S.Y.; Poges, S.; Jafari, T.; Song, W.; Liu, J.; et al. Hierarchical mesoporous NiO/MnO2@ PANI core–shell microspheres, highly efficient and stable bifunctional electrocatalysts for oxygen evolution and reduction reactions. *ACS Appl. Mater. Interfaces* **2017**, *9*, 42676–42687. [CrossRef]
69. Bhushan, M.; Mani, M.; Singh, A.K.; Panda, A.B.; Shahi, V.K. Self-standing polyaniline membrane containing quaternary ammonium groups loaded with hollow spherical $NiCo_2O_4$ electrocatalyst for alkaline water electrolyser. *J. Mater. Chem. A* **2020**, *8*, 17089–17097. [CrossRef]
70. Saddeler, S.; Bendt, G.; Salamon, S.; Haase, F.T.; Landers, J.; Timoshenko, J.; Rettenmaier, C.; Jeon, H.S.; Bergmann, A.; Wende, H.; et al. Influence of the cobalt content in cobalt iron oxides on the electrocatalytic OER activity. *J. Mater. Chem. A* **2021**, *9*, 25381–25390. [CrossRef]

71. Wang, C.; Wang, R.; Peng, Y.; Chen, J.; Chen, Z.; Yin, H.; Li, J. Nb-incorporated Fe (oxy) hydroxide derived from structural transformation for efficient oxygen evolution electrocatalysis. *J. Mater. Chem. A* **2020**, *8*, 24598–24607. [CrossRef]
72. Ouyang, T.; Ye, Y.Q.; Wu, C.Y.; Xiao, K.; Liu, Z.Q. Heterostructures composed of N-doped carbon nanotubes encapsulating cobalt and β-Mo2C nanoparticles as bifunctional electrodes for water splitting. *Angew. Chem. Int. Ed.* **2019**, *58*, 4923–4928. [CrossRef]